Dynamic Behavior of Rippled Shock Waves and Subsequently Induced Areal-Density-Perturbation Growth in Laser-Irradiated Foils

T. Endo,* K. Shigemori, H. Azechi, A. Nishiguchi,[†] K. Mima, M. Sato, M. Nakai, S. Nakaji, N. Miyanaga, S. Matsuoka, A. Ando, K. A. Tanaka,[‡] and S. Nakai

Institute of Laser Engineering, Osaka University, 2-6 Yamada-oka, Suita, Osaka 565, Japan
(Received 8 August 1994)

Polystyrene foils with surface ripples of 60 or 100 μm wavelength were irradiated by 0.53 μm laser light at an intensity of 4×10^{13} W/cm^2. Phase inversion of the rippled shock front was observed at a shock-propagation distance equal to the ripple wavelength. It has been found that the growth of the areal-density perturbation prior to shock breakout is due predominantly to the rippled-shock propagation.

PACS numbers: 52.35.Py, 52.35.Tc, 52.50.Jm

The study of hydrodynamical perturbation growth in the shock-compression phase is essential for a better understanding of the Rayleigh-Taylor (RT) instability [1] not only in inertial-confinement-fusion (ICF) implosions [2,3] but also in supernova explosions [4]. When ablation pressure is first applied on an ICF target with surface ripples, a rippled shock wave is launched in accordance with the target surface. It is predicted that once a shock front is rippled the amplitude of the ripple tends to oscillate as the shock propagates [5,6]. This is caused by lateral fluid motion behind the shock front. The oscillation of the rippled shock would amplify target perturbations and determine the initial conditions on the RT instability after shock breakout [7–9].

This Letter presents the first experimental observation of the dynamics of rippled shocks in plasmas. Sinusoidally rippled foils were uniformly irradiated by partially coherent light, and the following three quantities were measured: ripples of the shock front, perturbations of areal density, and ripples of the laser-irradiated surface. The experimental results have shown that the areal-density perturbations grow as a result of the propagation of the rippled-shock front, whereas the ripples at the ablation front of the laser-irradiated surfaces do not (prior to shock breakout). These results are well reproduced by two-dimensional computer simulations.

The experimental arrangement is shown in Fig. 1. Planar targets were made of polystyrene (PS) with a density of 1.06 g/cm^3 and a thickness of either 40 or 80 μm. The laser-irradiation surface of the target was sinusoidally rippled. The wavelength of the ripples was either 60 or 100 μm, and their initial amplitudes ranged from 2 to 8 μm. The PS target was glued on a Be substrate with a rectangular (0.8 $\times$ 0.8 mm^2 or 0.4 $\times$ 0.8 mm^2) diagnostic window. The initial ripple of each target was characterized with contact profilometry. Fourier amplitudes of the second and third harmonics were less than 0.1 and 0.03 of the fundamental amplitude, respectively. For uniform laser irradiation, we used frequency-doubled (0.53 μm) fiber-generated partially coherent light (PCL) [10] with a random-phase plate [11] implemented in the

GEKKO-XII Nd:glass laser facility [12]. The characteristics of the frequency-doubled PCL were a bandwidth of 0.2 nm, a beam divergence of 130 μrad (64 times diffraction limit), and a one-dimensional angular dispersion of 478 μrad/nm. The speckled pattern produced by the random-phase plate was smoothed out two dimensionally in an averaging time of 20 ps. The target was irradiated at an intensity of 4×10^{13} W/cm^2 and an incidence angle of 31.7° from the target normal. The time-integrated focal pattern had a bell shape with a 2.4% (rms) fluctuation from the smooth envelope. The diameter of the flat portion was approximately 300 μm, over which the intensity decreased by 15% from the maximum. The temporal laser-pulse shape was flat topped, where the FWHM was 2.2 ns, the rise time was 0.1 ns, and the fall time was 0.25 ns. The time $t = 0$ in this paper is defined as the time when laser intensity rises to half maximum.

The targets were diagnosed in three ways. First, ripples of the shock front were observed by optical emission due to shock breakout at the rear surface of the target. We used a Schwarzschild microscope with a magnification of 6.7, coupled to an S-20 streak camera with a band-pass filter of 380–480 nm wavelength. Spatial and temporal resolutions were approximately 8 μm and 70 ps, respectively. Second, perturbations of areal density were observed by face-on x-ray backlighting using Ge x-ray backlighters producing 1.6–1.8 keV x rays. We used an
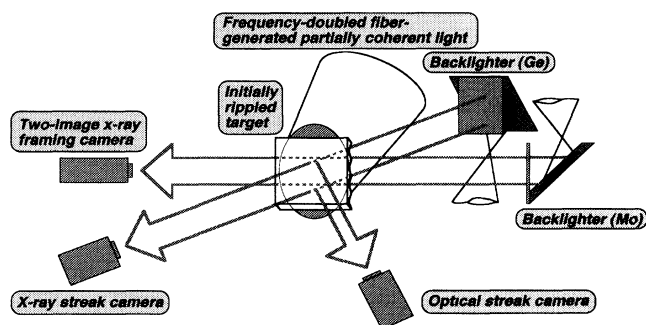

FIG. 1.   Schematic view of the experimental arrangement.

0031-9007/95/74(18)/3608(4)$06.00

x-ray pinhole camera with a 10 × 80 μm² imaging slit and with a magnification of 28, coupled to an x-ray streak camera with a 5-μm-thick Si filter. We used a Au photocathode for thinner targets and a CuI photocathode for thicker targets. For a soft-x-ray shield, a 10-μm-thick Be foil was placed between the target and the backlighter. The effective absorption coefficients of the targets for the broadband backlighters were calibrated around the target thicknesses used. The spatial resolution was measured using backlit gold-grid images to be approximately 10 and 12 μm for the Au and CuI photocathodes, respectively. Temporal resolution of the x-ray streak camera was approximately 90 ps. Third, ripples of laser-irradiated surfaces were observed by side-on x-ray backlighting using Mo x-ray backlighters generating 2.5–2.9 keV x rays. We used an x-ray pinhole camera with 5-μm-diameter pinholes and with a magnification of 30, coupled to a two-image x-ray framing camera with a 20-μm-thick Be filter prior to a CuI photocathode. Again for a soft-x-ray shield, a 10-μm-thick Be foil was placed between the target and the backlighter. The spatial resolution was also measured to be approximately 5 μm. The temporal resolution was approximately 100 ps. Charge-coupled device (CCD) cameras were used to record the streak- and framing-camera images. All values of the spatial resolution described above are those at the target position. The time origin $t = 0$ for each shot was established from time-fiducial signals in the shock measurement and the side-on measurement, and from a sharp rise of the backlighter emission in the face-on measurement.

Figure 2(a) shows a streaked image of the shock-breakout emission at the rear surface. It is seen that the emission intensity sharply rises and gradually decays, consistent with the shock breakout followed by rarefaction and expansion at the rear surface. The long emission at the left and right ends to the image is due to interaction of the shock-accelerated target material with the Be window edge. Thus the long emission can be used as a spatial fiducial signal. The relation of the spatial phase between the initial and observed ripples is, therefore, reliably known from the position with respect to the window edge. Moreover, before the shot, the target was placed at the right position, then imaged on the S-20 streak camera so that the initial ripple phase was readily known on the same CCD screen as that at the shot. The accuracy of the spatial-phase observation was better than ±7% of the ripple wavelength. By inspecting the spatial correspondence of Fig. 2(a), it has been found that the shock wave traveling through the thicker portion of the target arrived at the rear surface earlier than that through the thinner portion, as denoted by the dashed lines. This is clear evidence of the phase inversion of the shock-front ripple.

From the time history of the shock emission, we determined the difference in the breakout times between the shock trough and crest at which the exposures were a constant fraction of their peaks. The ripple
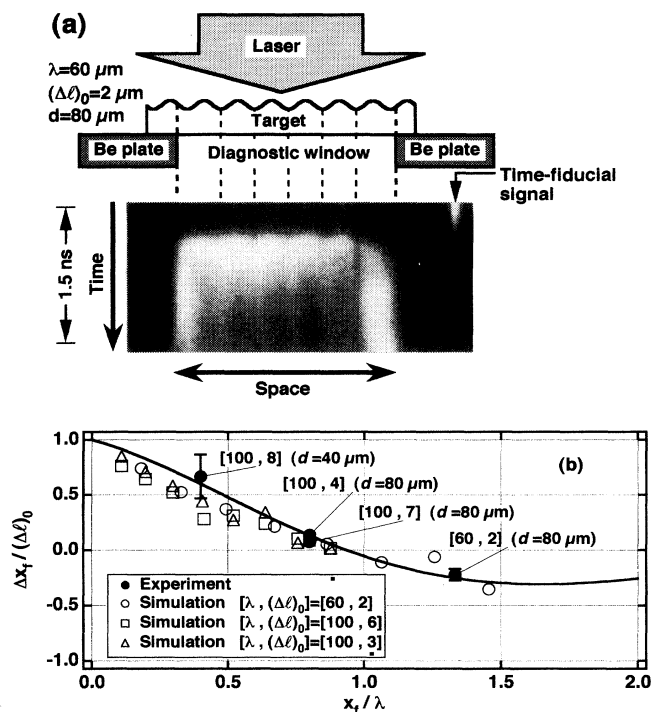

FIG. 2. (a) A streaked image of the shock-breakout emission, where λ, $(\Delta\ell)_0$, and d are the ripple wavelength, the initial amplitude of the surface ripple, and the target thickness, respectively. The white region in the image corresponds to the intense-emission region. (b) Evolution of the shock-front-ripple amplitudes, where Δx_f and x_f are the shock-front-ripple amplitude and the shock-propagation distance, respectively. Shown in brackets are λ and $(\Delta\ell)_0$ in μm. The curve in the figure is plotted only to show a trend of the data.

amplitude was determined by multiplying the shock velocity by the difference in the shock-breakout times. The shock velocity was measured using wedge targets to be $(3.5 \pm 0.2) \times 10^6$ cm/s. This corresponds to a shock pressure of 9 Mbar. The closed circles in Fig. 2(b) show the evolution of the shock-front-ripple amplitudes deduced by the described procedure above, where the shock-propagation distance x_f corresponds to the target thickness. The error bars include the spatial fluctuation of the ripple amplitude and uncertainties in the shock-velocity and shock-breakout-time measurements. Figure 2(b) suggests a damped oscillation in which a phase inversion occurs at a shock-propagation distance x_f of one ripple wavelength λ. Open plotting symbols in Fig. 2(b) show the results of the two-dimensional simulation code IZANAMI [13], and agree well with the experimental results.

In the following, the propagation of the ripple shock wave is analyzed by the shock-front ray trace. Let us consider ray tubes whose boundaries are determined by the trajectories of the shock front. When perturbations of a plane uniform shock wave are small enough, it has

been shown [14] that $(\partial u_s/\partial t)/u_{s0} = -(1/\alpha)(\partial A/\partial t)/A_0$, where u_s is the shock velocity in an imaginary ray tube, A is the ray-tube cross-sectional area, the subscript 0 denotes the initial unperturbed values, and α is a function of the shock strength and the specific-heat ratio [14]. Let the x and y axes be parallel to the shock-propagation direction and the wave-vector direction of the initial shock-front ripple, respectively, and $x_s = u_{s0}t + \xi_x(t, y)$ and $y_s = y + \xi_y(t, y)$ stand for the position of the shock front at time t, where $\xi_x(t, y)$ and $\xi_y(t, y)$ are the small deviations from the unperturbed position. Then by geometry, the following relations are obtained: $(1/A_0)(\partial A/\partial t) = (\partial/\partial t)(\partial \xi_y/\partial y)$ and $\partial \xi_y/\partial t = -u_{s0}(\partial \xi_x/\partial y)$. Using these relations and the relation between u_s and A, it can be found that the shock-front ripple $\xi_x(t, y)$ should satisfy the wave equation $\partial^2 \xi_x/\partial t^2 = (u_{s0}^2/\alpha)(\partial^2 \xi_x/\partial y^2)$. When the shock front initially has a sinusoidal ripple with a wavelength λ and an amplitude $(\Delta x_f)_0$, i.e., $\xi_x(0, y) = (\Delta x_f)_0 \cos[(2\pi/\lambda)y]$ and $\xi_y(0, y) = 0$, then the wave equation yields $\xi_x(t, y) = \Delta x_f \cos[(2\pi/\lambda)y]$, where $\Delta x_f = (\Delta x_f)_0 \cos[(2\pi/\lambda) \times (x_f/\alpha^{1/2})]$ for a shock-propagation distance $x_f = u_{s0}t$. This solution implies the oscillation of the rippled-shock amplitude and is qualitatively in agreement with the experimental observation. Quantitatively, however, for $\gamma = \frac{5}{3}$ and $M_0^2 \gg 1$ (γ is the specific-heat ratio, M_0 the Mach number of the unperturbed shock wave), the phase inversion is expected to occur at the shock-propagation distance $x_f/\lambda = 0.53$ though it occurred at $x_f/\lambda \approx 1$ in the experiment. Also the analytical solution does not show the damped oscillation. These discrepancies may be due to the lack of the ablation front in the analysis described above. It has been found by simulations that the pressure perturbation behind the shock front decreases through the ablation front during the shock propagation.

The ripple-shock propagation will introduce areal-density perturbations. They were measured with face-on x-ray backlighting. Figure 3(a) shows the evolution of the backlit spatial patterns. Each datum was temporally integrated for 0.1 ns. The areal-density-perturbation amplitude was iteratively obtained by taking account of the backlighter spatial structures, the measured resolution functions, and the measured effective absorption coefficients. By χ^2 minimization, both the backlighter structure and the areal-density perturbation were simultaneously determined. The backlighter structure was well fitted by a superposition of two Gaussian functions. Regarding the areal-density perturbation, we used the sinusoidal perturbation only of the fundamental. When the second harmonics were taken into account in the data reduction, the Fourier amplitude of the second harmonics was scattered around zero and the average amplitude was much smaller than the fundamental amplitude. Hence we judged that the deduced second harmonics were not real but rather originated from experimental artifacts such as quantum noise on the image. Simulation results shown
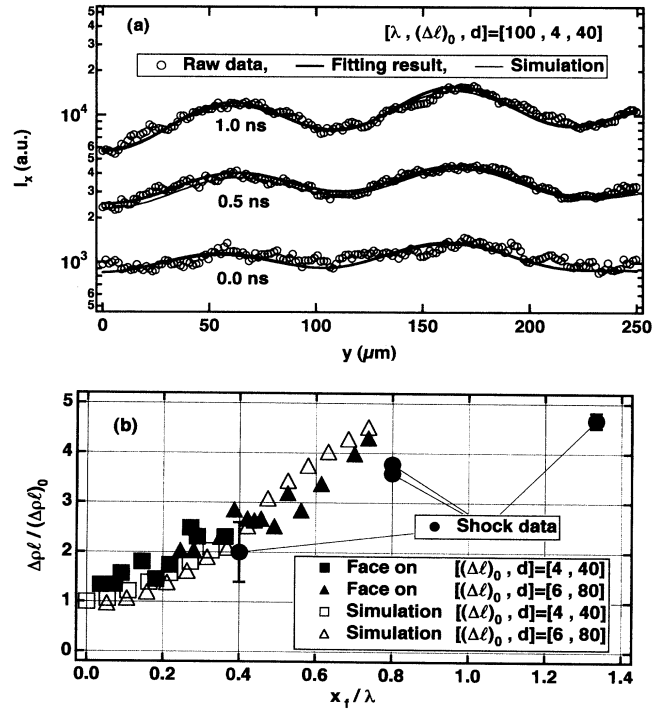

FIG. 3. (a) Temporal evolution of the backlit spatial patterns, where I_x, y, λ, $(\Delta\ell)_0$, and d are exposure, position, the ripple wavelength, the initial amplitude of the surface ripple, and the target thickness, respectively. Shown in brackets are λ, $(\Delta\ell)_0$, and d in μm. (b) Evolution of the areal-density-perturbation amplitudes, where $\Delta\rho\ell$, $(\Delta\rho\ell)_0$, and x_f are the areal-density-perturbation amplitude and its initial value, and the shock-propagation distance, respectively. The ripple wavelength λ was 100 μm except for the shock data. Shown in brackets are $(\Delta\ell)_0$ and d in μm.

in Fig. 3(a) also took account of both the instrumental resolution and the backlighter structures, and agree well with the experimental results. In Fig. 3(b), closed squares and triangles show the measured evolution of the areal-density perturbations, where the data are plotted until shock breakout. Errors in the experimental results are represented by the scatter of the data. The simulation results, shown by the open symbols in Fig. 3(b), agree well with the experimental results.

Since the areal-density perturbation can grow due both to the rippled-shock propagation and to the surface-ripple growth at the ablation front, it is necessary to measure the temporal evolution of the surface-ripple amplitude as well. We directly observed the surface ripples by side-on x-ray backlighting. In the side-on geometry, the laser-irradiated surface may be hidden by the surrounding weakly irradiated surface. To avoid this, the target width was restricted to be 300 μm over which the laser intensity decreased only by 15%. Figure 4(a) shows backlit images of the target. Iso-exposure contour plots were drawn to obtain the surface-ripple amplitudes. Figure 4(b) shows
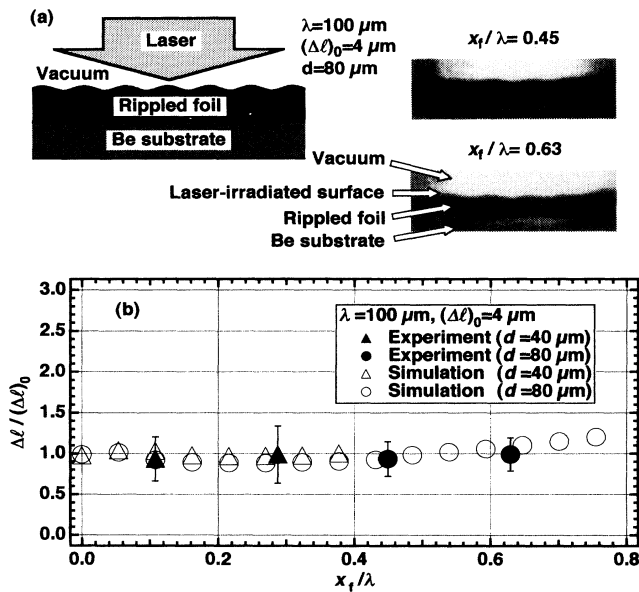
FIG. 4. (a) Backlit images of a target obtained by an x-ray framing camera in side-on geometry, where λ, $(\Delta\ell)_0$, d, and x_f are the ripple wavelength, the initial amplitude of the surface ripple, the target thickness, and the shock-propagation distance, respectively. Also shown is x_f/λ corresponding to the time of exposure. (b) Evolution of the surface-ripple amplitudes, where $\Delta\ell$ and $(\Delta\ell)_0$ are the surface-ripple amplitude and its initial value.

the evolution of the surface-ripple amplitudes. All data were taken prior to shock breakout. It is shown in Fig. 4(b) that the laser-irradiated-surface ripples do not grow prior to shock breakout in both the experiments and the simulations.

Since the surface ripples do not grow, we can evaluate the areal-density-perturbation amplitudes due solely to the propagation of the ripple shocks. If one makes a simplifying approximation that the shock-compressed density is spatially uniform, then the areal-density perturbation is given by $\rho_s[(\Delta\ell)_0 - \Delta x_f] + \rho_0\Delta x_f$, where Δx_f is the ripple amplitude of the shock front, ρ_s is the density behind the shock, ρ_0 is the initial density, and $(\Delta\ell)_0$ is the initial ripple amplitude at the surface. Using a density ratio for strong shock compression, $\rho_s/\rho_0 = 4$, we obtain the ratio of the areal-density perturbation to the initial one to be $\Delta\rho\ell/(\Delta\rho\ell)_0 = \Delta\rho\ell/\rho_0(\Delta\ell)_0 = 4 - 3\Delta x_f/(\Delta\ell)_0$. Thus the amplification of the areal-density perturbation may be deduced from the measured ripple amplitude Δx_f. This is shown in Fig. 3(b) by the closed circles. The areal-density-perturbation amplitudes evaluated from the rippled-shock data are consistent with those directly measured by the face-on x-ray backlighting. This implies that the areal-density-perturbation growth is due mainly to the

rippled-shock-front oscillation. The slight excess of the measured areal-density perturbations over the evaluated ones may be due to the density modulation behind the shock front created by the rippled-shock propagation.

In conclusion, we reported the first experiments on the dynamics of rippled shock waves and the resultant growth of areal-density perturbations in plasmas. It has been shown that a rippled-shock front oscillates when a rippled surface of a target is irradiated by a laser. The areal-density perturbation grows primarily due to the rippled shock-front oscillation until shock breakout. These hydrodynamic phenomena would determine the initial conditions for the Rayleigh-Taylor instability that occurs after shock breakout.

*Present address: Department of Microsystem Engineering, Nagoya University, Chikusa-ku, Nagoya 464-01, Japan.
†Present address: Osaka Institute of Technology, Omiya Asahi-ku, Osaka 535, Japan.
‡Permanent address: Faculty of Engineering, Osaka University, 2-1 Yamada-oka, Osaka 565, Japan.

[1] S. Chandrasekhar, Hydrodynamic and Hydromagnetic Stability (Oxford University Press, London, 1968), Chap. 10.
[2] J. Nuckolls et al., Nature (London) 239, 139 (1972).
[3] H. Takabe and T. Ishii, Jpn. J. Appl. Phys. 32, 5675 (1993).
[4] I. Hachisu et al., Astrophys. J. 390, 230 (1992).
[5] K. Meyer and P. Blewett, Phys. Fluids 15, 753 (1972).
[6] D. Munro, Phys. Fluids B 1, 134 (1989).
[7] H. Takabe et al., Phys. Fluids 28, 3676 (1985).
[8] J. Grun et al., Phys. Rev. Lett. 58, 2672 (1987); M. Desselberger et al., Phys. Rev. Lett. 65, 2997 (1990); S. Glendinning et al., Phys. Rev. Lett. 69, 1201 (1992).
[9] B. Remington et al., Phys. Rev. Lett. 67, 3259 (1991); Phys. Plasmas 2, 241 (1995).
[10] H. Nakano et al., Appl. Phys. Lett. 63, 580 (1993); N. Miyanaga et al., Bull. Am. Phys. Soc. 38, 2085 (1993).
[11] Y. Kato et al., Phys. Rev. Lett. 53, 1057 (1984).
[12] C. Yamanaka et al., Nucl. Fusion 27, 19 (1987).
[13] A. Nishiguchi and T. Yabe, J. Comput. Phys. 52, 390 (1983).
[14] G. Whitham, Linear and Nonlinear Waves (John Wiley and Sons, New York, 1974), Chap. 8. The function α, whose value is positive, is written as $[M_0^2/(M_0^2 - 1)] \times [1 + 2(1 - \mu^2)/(\gamma + 1)\mu][1 + 2\mu + 1/M_0^2]$, where M_0 is the Mach number of the unperturbed shock wave, γ is the specific-heat ratio, and μ is written as $\{[(\gamma - 1)M_0^2 + 2]/[2\gamma M_0^2 - (\gamma - 1)]\}^{1/2}$. When $M_0^2 \gg 1$, α becomes $(\gamma + 2)/\gamma + [2\gamma/(\gamma - 1)]^{1/2}$.
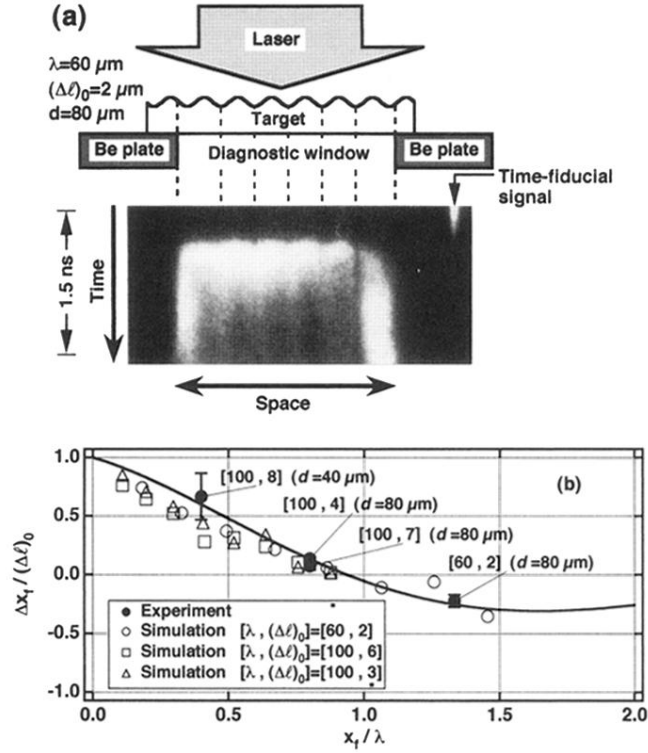
FIG. 2. (a) A streaked image of the shock-breakout emission, where λ, $(\Delta\ell)_0$, and d are the ripple wavelength, the initial amplitude of the surface ripple, and the target thickness, respectively. The white region in the image corresponds to the intense-emission region. (b) Evolution of the shock-front-ripple amplitudes, where Δx_f and x_f are the shock-front-ripple amplitude and the shock-propagation distance, respectively. Shown in brackets are λ and $(\Delta\ell)_0$ in μm. The curve in the figure is plotted only to show a trend of the data.
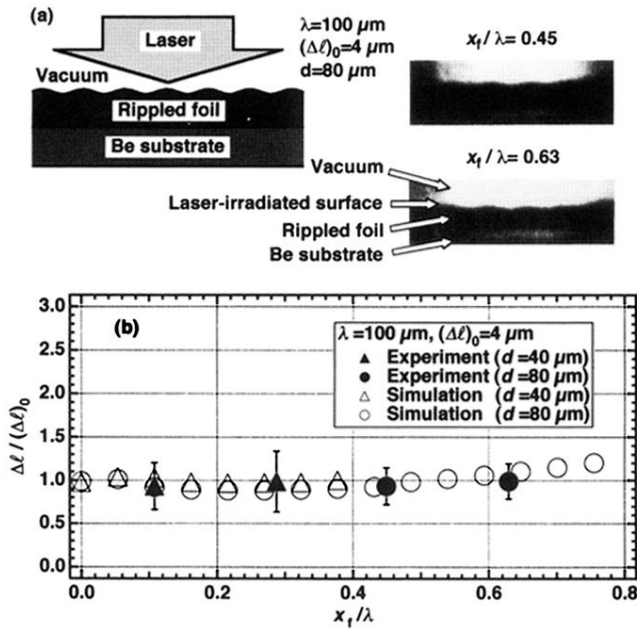
FIG. 4. (a) Backlit images of a target obtained by an x-ray framing camera in side-on geometry, where λ, $(\Delta\ell)_0$, d, and x_f are the ripple wavelength, the initial amplitude of the surface ripple, the target thickness, and the shock-propagation distance, respectively. Also shown is x_f/λ corresponding to the time of exposure. (b) Evolution of the surface-ripple amplitudes, where $\Delta\ell$ and $(\Delta\ell)_0$ are the surface-ripple amplitude and its initial value.